ScieRxiv
NOT PEER-REVIEWED
Research Article

# Synergistic photocatalytic $CO_2$ reduction on two-dimensional $TiO_2$ with Cu and ru dual single-atom sites

**Jeonghyeon Lee[1,†], Dongyun Kim[1,†], Junho Lee[1], Chaitanya B. Hiragond[1,2], Eunhee Gong[1], Su-Il In[1,*] and Yongfa Zhu[3]**

[1]Department of Energy Science & Engineering, DGIST, Daegu 42988, Republic of Korea.

[2]AI-Driven Hydrogen Technology Innovation Center (InnoCORE), Ulsan National Institute of Science and Technology (UNIST), Ulsan 44919, Republic of Korea.

[3]Department of Chemistry, Tsinghua University, Beijing 100084, China.

[†]These authors contributed equally to this work.

**Correspondence to:** Prof. Su-Il In, Department of Energy Science & Engineering, DGIST, Daegu 42988, Republic of Korea. E-mail: insuil@dgist.ac.kr

**Received: 04 September 2026 | Approved: 18 September 2026 | Online: 18 September 2026**

## Abstract

Photocatalytic $CO_2$ reduction offers a sunlight-driven route to convert a greenhouse gas into fuels. $TiO_2$ has been a well-established photocatalyst, but suffers from a wide bandgap, fast charge recombination, and weak $CO_2$ adsorption. Single-atom catalysts (SACs) address these limitations, yet dual single-atom catalysts (DSACs), pairing two distinct metal single atoms on one support, enhance the catalytic activity by increasing active sites and utilizing different metal properties. The large specific surface area of 2D $TiO_2$ can facilitate a higher loading of atomically dispersed metal species, thereby increasing activity. We report a Cu/Ru DSAC on 2D $TiO_2$ nanosheets that enhanced photocatalytic $CO_2$ reduction performance and stability by abundant atomic active sites

of Cu and Ru, improved $CO_2$ adsorption and light harvesting, and stabilization of reaction intermediates. Under gas-phase conditions, the optimized Cu/Ru DSAC (Cu 0.8 wt.%, Ru 0.6 wt.%) achieves a $CH_4$ evolution rate of 7.246 μmol $g^{-1}h^{-1}$, 49-fold higher than 2D $TiO_2$ and retains higher cyclic activity than the Cu-only catalyst. Under 7-sun condition, the $CH_4$ evolution rate further increases to 23.285 μmol $g^{-1}h^{-1}$. $^{13}CO_2$ isotopic labeling confirms the $CH_4$ carbon originates from the gas-phase feed. $CO_2$ temperature-programmed desorption (TPD) and *in situ* Diffuse reflectance infrared Fourier transform spectroscopy (DRIFTS) show that the Cu/Ru DSAC has a higher $CO_2$ chemisorption energy, converting $CO_2$ to $CH_4$ through carbonate/bicarbonate, *COOH, *CHO, $*CH_2O$, and $*CH_3O$ intermediates without detectable *CO accumulation. This work establishes dual single-atom catalyst as an effective strategy for enhancing photocatalytic $CO_2$ reduction.

**Keywords:** Dual single-atom catalysts, oxygen vacancy, 2D $TiO_2$ nanosheet, photocatalytic $CO_2$ reduction.

## INTRODUCTION

Atmospheric $CO_2$ concentration has continuously increased due to the extensive consumption of fossil fuels, contributing to various environmental problems[1,2]. Addressing these challenges requires reducing dependence on fossil fuels while expanding the use of renewable energy sources[3,4]. Among various $CO_2$ utilization strategies, catalytic $CO_2$ conversion provides a promising route for transforming $CO_2$ into value-added fuels and chemicals through thermocatalytic, electrocatalytic, and photocatalytic processes[5,6]. Photocatalytic $CO_2$ conversion directly utilizes solar energy under mild reaction conditions, making the development of efficient photocatalysts an attractive strategy for sustainable $CO_2$ utilization[1,2,5-9].

$TiO_2$ is one of the most widely studied photocatalysts because of its high photochemical stability, abundance, low cost, and favorable photocatalytic properties[7]. However, its wide bandgap of approximately 3.2 eV limits light absorption primarily to the ultraviolet region of the solar spectrum[10]. Its photocatalytic performance is further limited by inefficient charge separation, rapid electron-hole recombination, and relatively poor electrical conductivity[11]. To overcome these limitations, various strategies have been developed, including surface and defect engineering, morphology

control, heterojunction construction, and cocatalyst modification[12-19]. These include non-metal doping such as N- and B-doped $TiO_2$[20-22], heterojunction or Z-scheme architectures incorporating metal chalcogenide or copper oxide co-catalysts[23-25], nanotube or nanofiber morphologies combined with graphene-based or noble-metal co-catalysts[26-28], and defect/vacancy engineering via chemical or thermal reduction of $TiO_2$[29-32]. Atomically dispersed metal cocatalysts, commonly referred to as single-atom catalysts (SACs), maximize metal utilization by exposing isolated active sites and can promote charge separation through interfacial electron transfer between the semiconductor support and metal centers. Their distinct coordination environments also provide unique geometric and electronic structures that differ from those of nanoparticles or bulk metals[33-35]. The metal-support interaction is therefore a key factor governing the electronic structure, photocatalytic activity, and stability of SACs.

Cu is an earth-abundant transition metal that has attracted considerable attention for photocatalytic $CO_2$ reduction because of its favorable binding energies toward $CO_2$ and key reaction intermediates[36]. Atomically dispersed Cu species can stabilize metal-support interfaces through partially oxidized Cu sites, while simultaneously promoting the formation of adjacent oxygen vacancies. These oxygen vacancies can act as Lewis basic sites that facilitate $CO_2$ chemisorption[37]. Upon light irradiation, adsorbed $CO_2$ can undergo sequential reduction to surface intermediates such as *CHO and *CO, which are subsequently converted into hydrocarbon products[36,38]. Ru is another promising metal cocatalyst for photocatalytic $CO_2$ reduction because of its favorable electronic and catalytic properties. The incorporation of Ru can introduce additional electronic states within the bandgap, thereby extending light absorption into the visible region[39]. Ru also exhibits strong affinity toward CO-containing intermediates and high hydrogenation activity, while its ability to promote hydrogen activation and spillover can facilitate deep hydrogenation toward $CH_4$[40-43]. We hypothesized that pairing Cu-induced oxygen vacancies, which promote $CO_2$ chemisorption and stabilize *CO intermediates, with Ru-mediated hydrogen spillover and enhanced visible-light absorption would create dual active sites exhibiting strong synergy between Cu and Ru.

Herein, we report a dual single-atom catalyst (DSAC), atomically dispersed Cu and Ru on a 2D $TiO_2$ nanosheet support for photocatalytic $CO_2$ reduction into $CH_4$. The Cu and

Ru single-atom sites were sequentially introduced through a photochemical defect-tuning strategy involving oxygen vacancies in $TiO_2$[44]. This dual-site strategy was investigated as a means of improving charge separation, $CO_2$ activation, and photocatalytic performance through the complementary roles of Cu and Ru. High-angle annular dark-field scanning transmission electron microscopy (HAADF-STEM) and X-ray Absorption Fine Structure (XAFS) analyses were employed to determine the atomically dispersed metal on the 2D $TiO_2$. Combined X-ray photoelectron spectroscopy (XPS), Electron paramagnetic resonance (EPR), and Photoluminescence (PL) analyses reveal defect formation and modulation induced by Cu and Ru incorporation, suggesting improved charge-separation behavior. $CO_2$-Temperature-programmed desorption (TPD) and *in situ* diffuse reflectance infrared Fourier transform spectroscopy (DRIFTS) analysis were further employed to understand the adsorption behavior and surface reaction intermediates during the photocatalytic $CO_2$ reduction.

## EXPERIMENTAL

### Chemicals

Sodium hydroxide (NaOH, 93 %; Duksan Pure Chemicals Co., Ltd.), hydrochloric acid (HCl, 35 %; Daejung Chemicals & Metals Co., Ltd.), $TiO_2$ (P25, Degussa Chemicals Co., Ltd.), methyl alcohol ($CH_3OH$, 99.5 %; Daejung Chemicals & Metals Co., Ltd.), Copper(II) chloride dihydrate ($CuCl_2 \cdot 2H_2O$, 99.0%; Sigma Aldrich), and Ruthenium(III) chloride hydrate ($RuCl_3 \cdot xH_2O$, 99.9%, Sigma Aldrich) were used without further purification.

### Synthesis of 2D $TiO_2$ nanosheet

We synthesized 2D $TiO_2$ from P25 by the hydrothermal method[45]. 1 g of P25 was dissolved in 6 M NaOH aqueous solution and heated at 180 ℃ for 12 h in a Teflon-lined autoclave. After the reaction, the product was washed with 10 M HCl solution, and the precipitate was washed with deionized water and ethanol and collected by centrifugation. After freeze-drying, we annealed at 400 ℃ for 3h in air and obtained 2D $TiO_2$ nanosheets.

### Synthesis of Cu/2D $TiO_2$ and CuRu/2D $TiO_2$

We synthesized Cu/2D $TiO_2$ by utilizing the photochemical tun ing method[44]. 50 mg of 2D $TiO_2$ was dispersed in 10 mL of 20% methanol, and different amounts of $CuCl_2$ were dissolved in 5 mL of deionized water to prepare 0.2, 0.4, 0.6, 0.8, and 1.0 wt.% samples. Cu loadings (wt.%) were defined as the mass of elemental Cu relative to the mass of 2D $TiO_2$ (50 mg). The corresponding amounts of $CuCl_2 \cdot 2H_2O$ dissolved in 5 mL of deionized water were 2.7, 5.4, 8.1, 10.8, and 13.5 mg for the 0.2, 0.4, 0.6, 0.8, and 1.0 wt.% samples, respectively, of which 0.5 mL was used per synthesis. Two solutions were sonicated for 10 min, and purged with Ar for 10 min. After purging, 2D $TiO_2$ dispersion was irradiated by 1 sun using a 100 W xenon lamp with stirring at 200 RPM for 20 min. The 0.5 mL of Cu precursor was injected to photoreduced 2D $TiO_2$ dispersion by syringe and stirred at 500 RPM for 10 min. After this reaction, the precipitate was washed with deionized water and ethanol and collected by centrifugation. After drying in a vacuum oven at 60 ℃ for 12 h, we obtained Cu/2D $TiO_2$.

CuRu/$TiO_2$ was synthesized using the same method as Cu/2D $TiO_2$. The dried Cu/2D $TiO_2$ was dispersed in 10 mL of 20% methanol, and different amounts of $RuCl_3$ were dissolved in 5 mL of deionized water to prepare 0.2, 0.4, 0.6, 0.8, and 1.0 wt.% samples. Ru loadings (wt.%) were defined as the mass of elemental Ru relative to the mass of Cu/2D $TiO_2$ (50 mg). The corresponding amounts of $RuCl_3 \cdot xH_2O$ dissolved in 5 mL of deionized water were 2.5, 5.0, 7.5, 10.0, and 12.5 mg for the 0.2, 0.4, 0.6, 0.8, and 1.0 wt.% samples, respectively, of which 0.5 mL was used per synthesis. After the photochemical tuning method, the precipitate was washed with deionized water and ethanol and collected by centrifugation. After drying in a vacuum oven at 60 ℃ for 12 h, we obtained CuRu/2D $TiO_2$. Ru/2D $TiO_2$ was synthesized using the same method, but with 2D $TiO_2$ instead of Cu/2D $TiO_2$.

### Characterization

Field-emission transmission electron microscopy (FE-TEM) and high-angle annular dark-field scanning transmission electron microscopy (HAADF-STEM) images were recorded by ultra-high-resolution transmission electron microscopy (UHR-TEM) using Themis Z. X-ray absorption fine structure (XAFS) measurements were performed at the 10C beamline of the Pohang Light Source (3.0 GeV) using a double-crystal Si (111) monochromator and a Ge fluorescence detector. EXAFS data were processed using Demeter after background subtraction and normalization. X-ray diffraction (XRD) patterns were measured by a PANalytical Empyrean X-ray diffractometer (Rigaku) using Cu Kλ radiation (λ = 1.54 Å). The absorption spectra were recorded using an Agilent Cary series UV-visible near-infrared spectrophotometer with a diffuse reflectance accessory, in the range of 300-800 nm. Photoluminescence (PL) measurements were performed using a Cary Eclipse fluorescence spectrophotometer with an Agilent diffuse reflectance accessory, at an excitation wavelength of 320 nm. X-ray photoelectron spectroscopy (XPS) analysis was performed using a Thermo Scientific K-alpha X-ray photoelectron spectrometer using an Al Kα line (1,486.6 eV) as the X-ray source. Electron paramagnetic resonance (EPR) spectra were acquired using a Jeol JES-FA200 electron spin resonance spectrometer at 77 K. $CO_2$-Temperature-programmed desorption (TPD) measurements were conducted on an AutoChem II (Micromeritics). Samples were first exposed to $CO_2$ for adsorption and the desorption profiles were recorded under He flow.

**Photocatalytic $CO_2$ reduction**

We performed photocatalytic $CO_2$ reduction experiments using the experimental setup shown in Supplementary Figure 1. A 20 mg catalyst was dispersed on a glass substrate. The reactor was purged with moist $CO_2$ (1,000 ppm in He) by passing a bubbler at a 40 mL/min flow rate, and removed using a vacuum pump connected to the reactor. This cycle was repeated three times to remove gaseous impurities from the reactor. Finally, the reactor was filled with moist $CO_2$ and illuminated with a 100 W Xenon lamp (Oriel, LCS-100) with an AM 1.5 filter for the photocatalytic $CO_2$ reduction, and a 450 W lamp (AM1.5G, Oriel Sol3A) was used for the multi-sun effect experiment. The

gaseous products were taken from the reactor using a 500 µL syringe and injected into a gas chromatography unit (Shimadzu, GC2014) equipped with a thermal conductivity detector (TCD, Restek RT-Msieve 5A column, ID = 0.53 mm, length = 30 m) and a flame ionization detector (FID, Restek Rt-Q-bond column, ID = 0.53 mm and length = 30 m). The stability test was performed after light irradiation for 6 h and vacuum annealing at 100 ℃ for 2 h.

**Isotopic labeling experiments**

Isotopic labeling experiments were performed using $^{13}CO_2$ ($^{13}C$ 99%) diluted in pure He gas (99.999%) to form a 1,000 ppm concentration. A 20 mg catalyst was spread on a glass substrate and purged with moist pure He gas, and $^{13}CO_2$ was injected using a syringe and illuminated under a 100 W Xenon lamp. The gaseous products were analyzed during 6 h using gas chromatography-mass spectrometry (GC-MS, Shimadzu GC-MSQP2010 Ultra) equipped with a Restek Rt-Q-bond column (ID = 0.32 mm and length = 30 m).

***In situ* DRIFTS measurements**

Diffuse reflectance infrared Fourier transform spectroscopy (DRIFTS) was employed to probe surface intermediates formed during the reaction. *In situ* DRIFTS measurements were conducted using a Nicolet iS50 spectrometer (Thermo Fisher Scientific) equipped with a Praying Mantis reaction chamber (HVC-DRM) and a mercury-cadmium-telluride (MCT) detector [Supplementary Figure 2]. Before testing, the sample was heated to 100 °C in a vacuum for 2 h to remove the adsorbed molecules. Before illumination, the FTIR chamber was purged three times with $CO_2$ and $H_2O$ vapor and subsequently filled with the reactant mixture. Subsequently, they were exposed to $CO_2$ and $H_2O$ for 30 min, followed by light irradiation to acquire spectra. Spectra were collected in the dark and at defined time intervals under Xe lamp illumination. Each spectrum was averaged over 32 scans with a resolution of 4 $cm^{-1}$.

## RESULTS AND DISCUSSION

Figure 1A illustrates the synthesis route used to prepare the dual single-atom catalyst (DSAC). 2D $TiO_2$ nanosheets, obtained by NaOH-mediated hydrothermal treatment of P25, were sequentially photodeposited with Cu and then Ru metals. We followed a photochemical defect-tuning strategy in which oxygen vacancies generated under illumination migrate to the surface and provide anchoring sites for the incoming metal precursor[44]. Cu was deposited prior to Ru, consistent with reports that Cu single atoms on $TiO_2$ spontaneously induce adjacent oxygen-vacancy formation[37]. It provides a plausible structural basis for the subsequent dispersion of Ru. HR-TEM image in Figure 1B shows the nanosheet morphology of the parent 2D $TiO_2$ support. The dark, high-contrast spots observed in the image are attributed to Au originating from TEM grid as shown in Supplementary Figure 3A. The preserved morphology after Cu and Ru photodeposition are shown in Supplementary Figure 3B-D, with visible lattice fringes indicating that crystallinity is retained throughout metal loading. HAADF-STEM images of Cu/2D $TiO_2$, Ru/2D $TiO_2$, and CuRu/2D $TiO_2$ in Figure 1C-E show bright, atomically sized contrast points dispersed across the nanosheet surface without larger nanoparticle-like features, suggesting that Cu and Ru are present in a highly dispersed, near-atomic state.

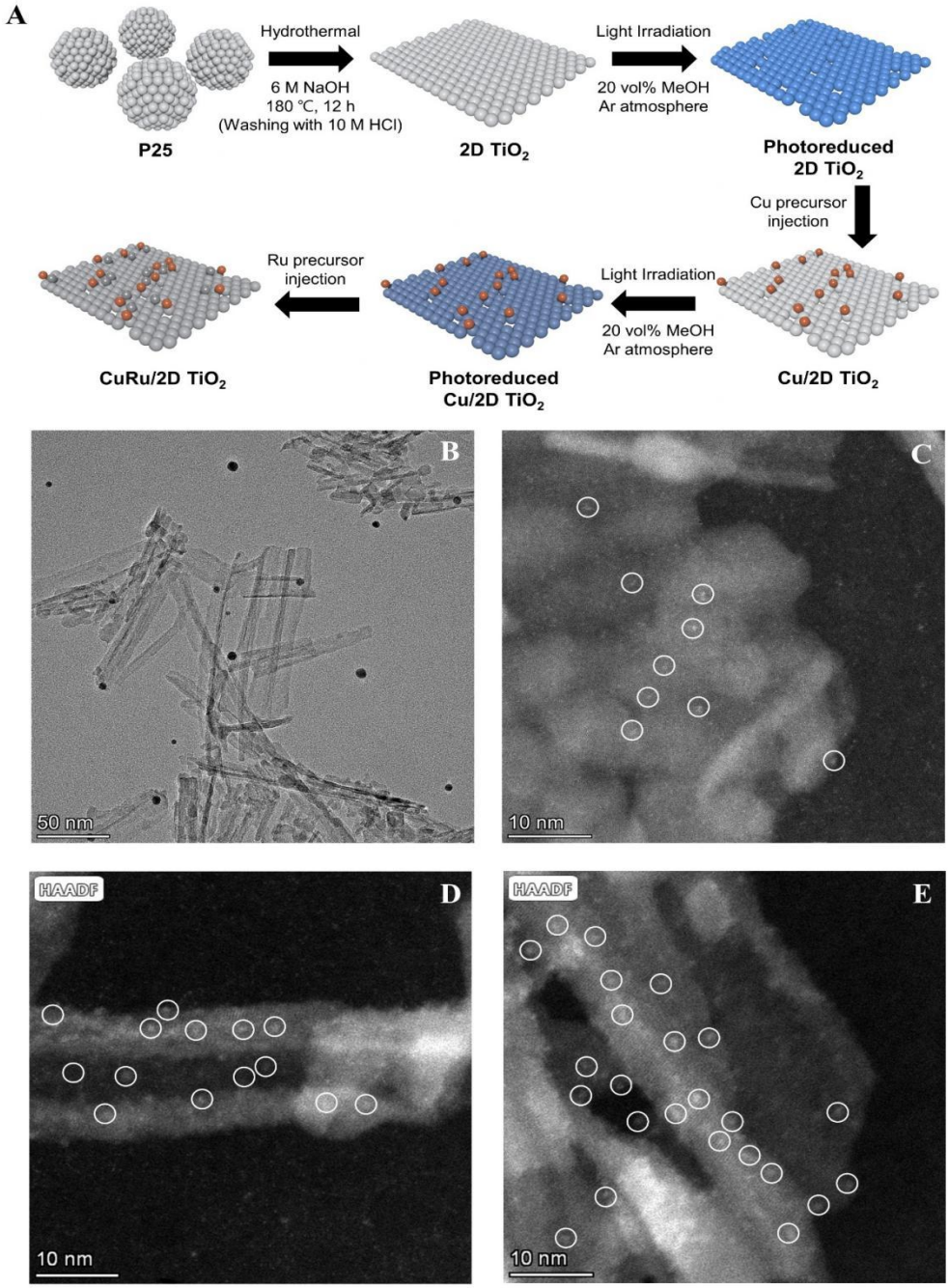


**Figure 1.** A, Schematic illustration of the synthesis process for 2D $TiO_2$, Cu/2D $TiO_2$, and CuRu/2D $TiO_2$; B, HR-TEM image of 2D $TiO_2$; HAADF-STEM images of C, Cu/2D $TiO_2$; D, Ru/2D $TiO_2$; and E, CuRu/2D $TiO_2$.

To determine the oxidation state and local coordination environment of the deposited metals prior to reaction, Cu and Ru K edge XAFS were collected for the fresh catalysts in Figure 2. The Cu K edge XANES spectra of Cu/2D $TiO_2$ and CuRu/2D $TiO_2$ closely resemble that of the CuO reference [Figure 2A], and the Ru K edge XANES spectra of

Ru/2D $TiO_2$ and CuRu/2D $TiO_2$ resemble that of $RuO_2$ [Figure 2B]. It indicates that Cu and Ru are present predominantly as $Cu^{2+}$ and $Ru^{4+}$ like species, respectively. Fourier-transformed EXAFS spectra in Figure 2C and D show a single dominant peak near 1.4 Å, assigned to Cu-O and Ru-O scattering, for all Cu- and Ru-containing samples, with no peak at the longer distances expected for Cu-Cu or Ru-Ru bonding in the corresponding metal foil references. Wavelet-transform EXAFS in Figure 2E confirms this in two dimensions: the k-R intensity maxima for Cu/2D $TiO_2$, Ru/2D $TiO_2$, and CuRu/2D $TiO_2$ fall at comparatively low k, consistent with the lighter O backscatterer, whereas the Cu foil and Ru foil references show maxima at substantially higher k. Together with HAADF-STEM results, we suggest that Cu and Ru are dispersed as isolated, oxygen-coordinated single atoms rather than as metallic or oxide nanoparticles[37,46].

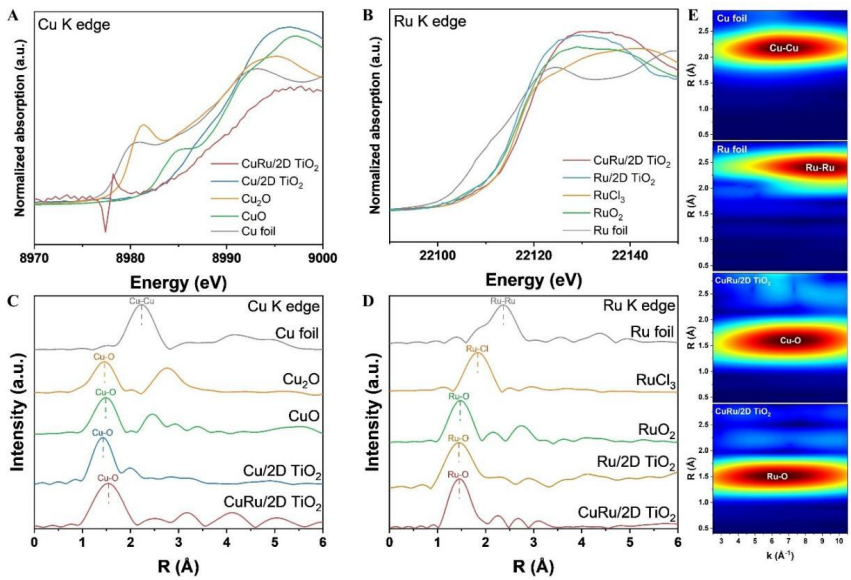


**Figure 2.** XANES spectra of A, Cu K edge; and B, Ru K edge; FT-EXAFS spectra of C, Cu K edge; and D, Ru K edge; E, WT-EXAFS spectra of Cu and Ru K edge $Cu_2O$, CuO, $RuCl_3$, and $RuO_2$.

Powder XRD patterns of all five samples match the anatase $TiO_2$ reference pattern in Figure 3A. P25 additionally shows a small reflection near 27.4°, corresponding to the (110) plane of rutile, which is absent in 2D $TiO_2$ and in all Cu-, Ru-, and CuRu-loaded samples. It indicates that the NaOH-mediated hydrothermal treatment and subsequent calcination convert the mixed-phase P25 into single-phase anatase nanosheets. No diffraction peaks attributable to metallic Cu, Ru, or their oxides are observed in the

metal-loaded samples, consistent with the absence of metal-metal scattering paths. The absence of metal-related diffraction peaks suggests that the atomically dispersed metal species do not significantly perturb the $TiO_2$ crystal structure or are present below the detection limit of XRD due to their low loading.

UV-Vis DRS spectra in Figure 3B show that Cu, Ru, and CuRu loading progressively increases visible-light absorption relative to P25 and 2D $TiO_2$. Tauc plot analysis is used to calculate the bandgap; see Supplementary Figure 4. This narrowing upon metal loading is consistent with the formation of mid-gap states within the $TiO_2$ bandgap, as reported computationally for single-atom Cu/$TiO_2$ and Ru/$TiO_2$ systems[39,47]. The additional weak absorption above ~700 nm observed for Cu-containing samples is consistent with the characteristically narrow bandgap (1.35-1.7 eV) reported for CuO-like local coordination environments[48].

Photoluminescence (PL) spectra in Figure 3C show emission intensity decreasing in the SAC and DSAC, with the Ru/2D $TiO_2$ and CuRu/2D $TiO_2$ curves nearly overlapping. This trend is consistent with progressively suppressed radiative electron-hole recombination upon nanosheet formation and metal loading, in agreement with reports that isolated Ru and Cu single atoms on $TiO_2$ can act as electron-trapping or electron-extracting sites that quench PL emission[49,50].

X-ray photoelectron spectroscopy (XPS) shows that the Ti 2p and O 1s binding energies of Cu/2D $TiO_2$ and CuRu/2D $TiO_2$ are shifted to lower energy relative to P25, 2D $TiO_2$, and Ru/2D $TiO_2$ [Figure 3D and E], consistent with $Cu^{2+}$-induced charge compensation promoting the formation of $Ti^{3+}$ and associated oxygen vacancies, as reported for related Cu/$TiO_2$ systems[45,51]. The Cu $2p_{3/2}$ binding energy decreases by approximately 0.53 eV upon Ru co-loading [Figure 3F], and the Ru $3d_{5/2}$ region of CuRu/2D $TiO_2$ shows a shoulder feature at a lower binding energy than the corresponding region of Ru/2D $TiO_2$ [Figure 3G]; together, these shifts suggest an electronic interaction between the co-loaded Cu and Ru sites. Valence-band XPS in Figure 3H shows that the valence band maximum (VBM) of Cu/2D $TiO_2$ has shifted to a more negative value, whereas Ru-loaded samples shifted to more positive values. The incorporation of Cu single atoms introduces Cu-derived electronic states within the bandgap of $TiO_2$[47]. In particular, the hybridization of Cu 3d and O 2p orbitals can

generate occupied states above the pristine $TiO_2$ valence-band edge, resulting in an apparent decrease in the VB-XPS onset energy[37,52]. The VBM of Ru-loaded catalysts was increased, indicating a downward shift of the valence-band edge. This is consistent with strong Ru-O-Ti electronic coupling and interfacial charge redistribution, as reported for atomically dispersed Ru on $TiO_2$[49].

EPR spectra in Figure 3I show no detectable signal for P25 or 2D $TiO_2$, consistent with the low density of paramagnetic $Ti^{3+}$ centers expected in unmodified $TiO_2$. Cu/2D $TiO_2$ shows a signal at g = 2.05, assigned to $Cu^{2+}$ in a local coordination environment similar to that reported for single-atom $Cu/TiO_2$[47], and Ru/2D $TiO_2$ shows a signal at g = 2.04 together with a minor shoulder at g = 1.998 [Supplementary Figure 11]; the g = 1.998 signal is consistent with the well-established $Ti^{3+}$ signal in anatase $TiO_2$[53]. The g = 2.04 signal falls in the range reported for surface-bound, dissociative $O^-$ species in a Ru-modified oxygen environment[49,54]. CuRu/2D $TiO_2$ shows an intermediate signal at g = 2.045, most conservatively interpreted as an unresolved overlap of the $Cu^{2+}$ and Ru-related signals rather than a distinct new chemical species, given the spectral resolution available.

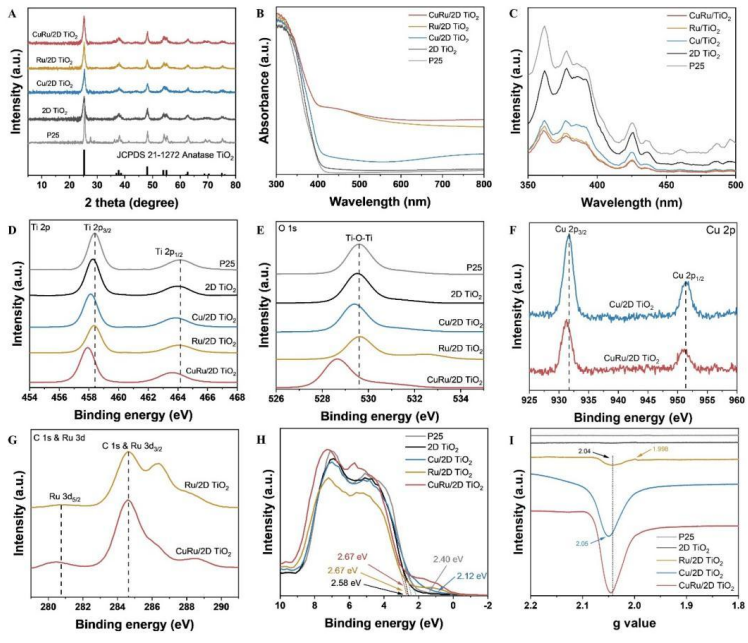


**Figure 3.** A, XRD patterns; B, UV-VIS DRS spectra; C, PL spectra; XPS analysis of D, Ti 2p; E, O 1s; F, Cu 2p; G, C 1s and Ru 3d; H, Valence band XPS patterns; and I, EPR analysis of P25, 2D $TiO_2$, Cu/2D $TiO_2$, Ru/2D $TiO_2$, and CuRu/2D $TiO_2$.

Photocatalytic $CO_2$ reduction activity was evaluated under gas-phase conditions (1,000

ppm wet $CO_2$, 1 sun). Screening the Cu loading in Cu/2D $TiO_2$ in Figure 4A identified 0.8 wt.% Cu as optimal, giving a $CH_4$ evolution rate of 4.696 μmol $g^{-1}h^{-1}$ with minor $C_2H_4$ and $C_2H_6$ (0.149, 0.020 μmol $g^{-1}h^{-1}$, respectively) co-products as calculated during the first hour. This optimum is close to the 0.75 wt.% Cu loading reported for a related Cu-loaded $TiO_2$ nanosheet system, in which loadings beyond the optimum were attributed to blocking of active sites and reduced $CO_2$ adsorption[45]. With Cu fixed at 0.8 wt.%, screening the Ru co-loading in CuRu/2D $TiO_2$ in Figure 4B identified 0.6 wt.% Ru as optimal, giving a $CH_4$ evolution rate of 7.246 μmol $g^{-1}h^{-1}$, which is 77 and 49 times higher than P25 and 2D $TiO_2$, respectively [Supplementary Figure 12], with minor $C_2H_4$ and $C_2H_6$ (0.129, 0.074 μmol $g^{-1}h^{-1}$, respectively). Ru also showed lower activity beyond the optimum loading condition due to the blocking of active sites. We performed multi-sun illumination for the photocatalytic activity of CuRu/2D $TiO_2$ [Figure 4C]. Increasing the light intensity enhanced $CO_2$ reduction activity, reaching a maximum of 28.671 μmol $g^{-1}h^{-1}$ at 7-sun illumination for 1 hr. Increased photon flux under higher irradiance generated a large population of photogenerated charge carriers, enhancing photocatalytic activity. Under the 9-sun condition, a decrease in photocatalytic activity was observed, likely due to enhanced charge-carrier recombination resulting from the excessive accumulation of photogenerated electrons and holes at high light intensity[55].

Over 6 h of continuous irradiation, CuRu/2D $TiO_2$ accumulated 23.285 μmol $g^{-1}$ $CH_4$, compared with 12.34 μmol $g^{-1}$ for Cu/2D $TiO_2$, while Ru/2D $TiO_2$ and Cu/2D $TiO_2$ activity plateaued after roughly 3 and 4 h, respectively, in Figure 4D. CuRu/2D $TiO_2$ instead increased approximately linearly for the first 2 h before its rate gradually declined; it shows longer-term activity than other catalysts. Catalyst stability was assessed over four successive 6 h cycles with intermediate thermal regeneration (100 °C, vacuum, 2 h) as shown in Figure 4E. Cu/2D $TiO_2$ activity collapsed almost completely after the first cycle. CuRu/2D $TiO_2$ retained substantially more activity than Cu/2D $TiO_2$ but still declined markedly, falling to approximately 7.4 μmol $g^{-1}$ after the second cycle and to roughly 5-7% of its initial activity by the third and fourth cycles. It indicates that the atomically dispersed Cu and Ru sites may destabilize the metal-$TiO_2$ interactions, leading to the cleavage of metal-support bonds and consequent loss of active sites, thereby resulting in a decrease in photocatalytic activity[45]. In Figure 4F, a $^{13}CO_2$ isotopic test was performed to validate the carbon source for $CH_4$ production

during the photocatalysis. The formation of $^{13}CH_4$ at m/z = 17 was clearly detected over time, confirming the progressive generation of $^{13}CH_4$ during the photocatalytic reaction.

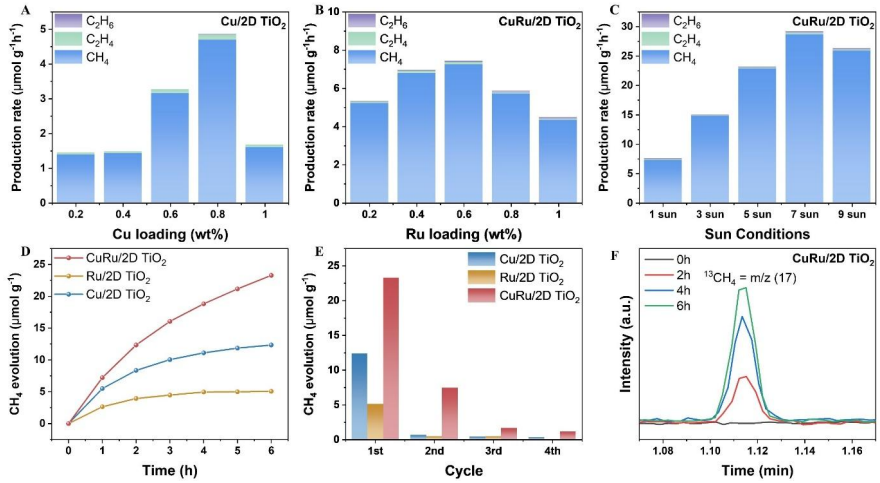


**Figure 4.** Photocatalytic $CO_2$ reduction performance of A, Cu/2D $TiO_2$ with varying Cu contents; and B, CuRu/2D $TiO_2$ with varying Ru contents; C, photocatalytic performance of CuRu/2D $TiO_2$ under different sun illuminations; D, time-dependent results; and E, stability test of Cu/2D $TiO_2$, Ru/2D $TiO_2$, and CuRu/2D $TiO_2$. (f) GC-MS chromatogram confirming $^{13}CH_4$ formation for CuRu/2D $TiO_2$.

To identify the structural origin of the activity loss observed in Figure 4E, *ex-situ* Cu and Ru K edge XAFS were collected for CuRu/2D $TiO_2$ before and after the photocatalytic reaction [Figure 5]. In Figure 5A-C, the Cu K edge of XANES, FT-EXAFS, and WT-EXAFS spectra of the used catalyst closely resemble those of the fresh catalyst, with no peak appearing at the Cu-Cu distance and k-position expected for metallic Cu. This indicates that Cu remains atomically dispersed after reaction. In Figure 5D-F, the Ru K edge of the used catalyst shows a new EXAFS feature near the Ru-Ru distance of the Ru foil reference. We confirmed this more clearly by WT-EXAFS, where a new intensity maximum appears close to the k-R position of the Ru foil reference. This indicates that a fraction of the Ru sites are reduced to a metallic, aggregated state during the reaction. This asymmetric behavior is consistent with the relative deactivation trend in Figure 4E, in which CuRu/2D $TiO_2$ retains higher activity than Cu/2D $TiO_2$ at every cycle even as both catalysts decline.

The distinct electronic behavior induced by Cu and Ru incorporation suggests that the two metal sites play different roles in modulating the charge-transfer properties on 2D $TiO_2$. The VB-XPS results in Figure 3H showed that the Cu-derived or defect-associated electronic states are located above the intrinsic $TiO_2$ valence band. In contrast, the incorporation of Ru caused a pronounced increase in the VBM binding energy, indicating substantial Ru-induced modification of the electronic structure and Fermi-level position of $TiO_2$. The PL results in Figure 3C showed that Ru-containing catalysts exhibited pronounced PL quenching compared with Cu/2D $TiO_2$, indicating a more efficient suppression of radiative recombination. The EPR spectra in Figure 3I further indicate the formation of Ru-related $O^-$ species in the Ru-containing catalysts. Taken together with the VB-XPS, PL, EPR, and *ex-situ* EXAFS results, these observations suggest that Ru-containing sites may contribute to electron-trapping centers and charge separation in CuRu/2D $TiO_2$. Ru incorporation substantially modifies the electronic structure of $TiO_2$ and may facilitate charge separation and the accumulation of photogenerated electrons at Ru-containing sites[49,56]. We suggest that excessive charges were accumulated at the Ru more than at Cu, promoting the reduction of Ru species to metallic Ru. In contrast, Cu sites remain protected from such over-reduction, allowing the active sites to be preserved and thereby contributing to enhanced photocatalytic stability.

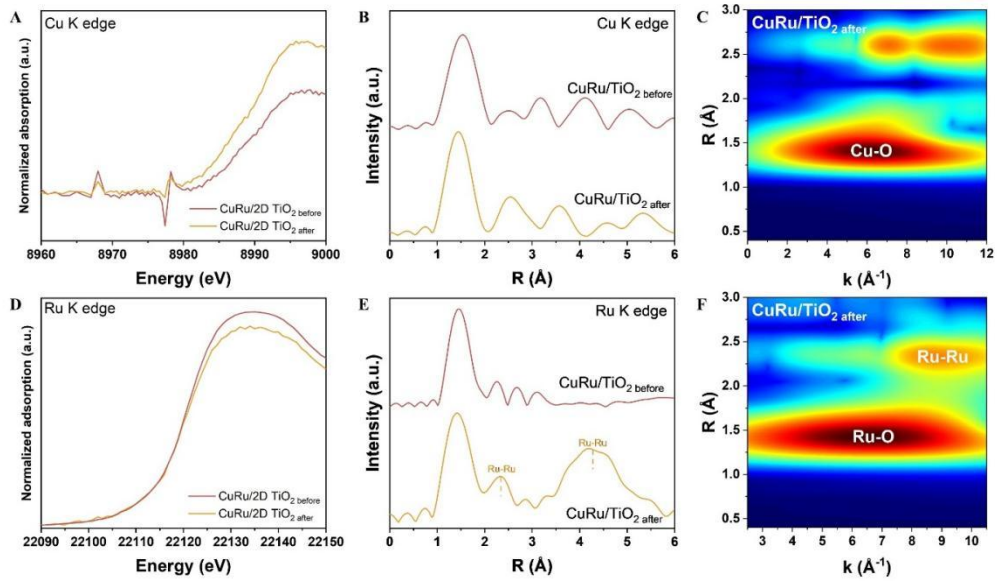


**Figure 5.** Cu K edge of A, XANES; B, FT-EXAFS; and C, WT-EXAFS; and Ru K edge of D, XANES; E, FT-EXAFS; and F, WT-EXAFS spectra before and after $CO_2$ reduction of CuRu/2D $TiO_2$.

$CO_2$-TPD [Figure 6A] shows no measurable $CO_2$ desorption from P25 or 2D $TiO_2$, consistent with the low density of Lewis basic oxygen-vacancy sites expected in the absence of metal loading. $CO_2$, a Lewis acid, requires such sites for chemisorption, and unmodified $TiO_2$ is computationally unfavorable for spontaneous oxygen-vacancy formation[37]. Cu/2D $TiO_2$ shows two chemisorption features at 321 and 383 °C. This is consistent with coordinatively unsaturated Cu sites and adjacent oxygen vacancies acting as Lewis acid-base pairs for $CO_2$/$H_2O$ adsorption, as reported for related Cu/reduced-$TiO_2$ photocatalysts[57]. Ru/2D $TiO_2$ shows a broader, lower-intensity feature at 410 °C together with a physisorption peak near 80 °C, and CuRu/2D $TiO_2$ shows the highest desorption temperature (416 °C). The higher desorption temperature of the Ru-containing samples relative to Cu/2D $TiO_2$ suggests a stronger $CO_2$ binding site. This is broadly consistent with reports that Ru-oxygen-vacancy sites specifically strengthen adsorbate binding relative to Ru sites without adjacent vacancies[58]. CuRu/2D $TiO_2$ shows both the highest desorption temperature and the most intense chemisorption feature among the five samples, tentatively suggesting it combines the strongest and abundant $CO_2$ chemisorption sites.

*In situ* DRIFTS of CuRu/2D $TiO_2$ under $CO_2$/$H_2O$ irradiation in Figure 6B-D shows time-dependent growth of a series of bands. The 1,200-1,800 $cm^{-1}$ region shows bands

assignable to monodentate and bidentate carbonate (1,236 and 1,589 $cm^{-1}$), bicarbonate (1,406, 1,450, and 1,697 $cm^{-1}$), adsorbed water (1,635 $cm^{-1}$), carboxyl (*COOH, 1,478 and 1,712 $cm^{-1}$), and formaldehyde-type (*$CH_2O$, 1,515 $cm^{-1}$) surface species, based on comparison with reported peak positions for the $TiO_2$ photocatalysts[45,59-63]. No band was detected in the 2,000-2,200 $cm^{-1}$ region expected for adsorbed *CO at any irradiation time, indicating that *CO does not accumulate as an observable surface intermediate. In the 2,500-3,200 $cm^{-1}$ region, three C-H stretching bands assignable to *CHO, *$CH_2O$, and *$CH_3O$ intermediates appear sequentially after approximately 60 min of irradiation, consistent with the *$CH_2O$ signal in the carbonyl region and indicating that the reaction proceeds through progressively hydrogenated C1 intermediates toward $CH_4$. These spectra support a reaction sequence in which $CO_2$ is first adsorbed as carbonate/bicarbonate species, converted to *COOH, and then hydrogenated through *CHO, *$CH_2O$, and *$CH_3O$ without observable *CO accumulation. The absence of a detectable *CO intermediate suggests that Cu strengthens *CO binding sufficiently to prevent its desorption or spectroscopic accumulation, promoting rapid further hydrogenation toward $CH_4$[45,46], while Ru is tentatively assigned a complementary role in water activation and proton supply[40-43]. Together with TPD and *in situ* DRIFTS results, we suggest that DSAC adsorbs $CO_2$ with higher binding energy, converting to a *CO intermediate by reacting with electrons and protons. The *CO intermediate stably binds to the catalyst surface and rapidly hydrogenates to form the $CH_4$ product.

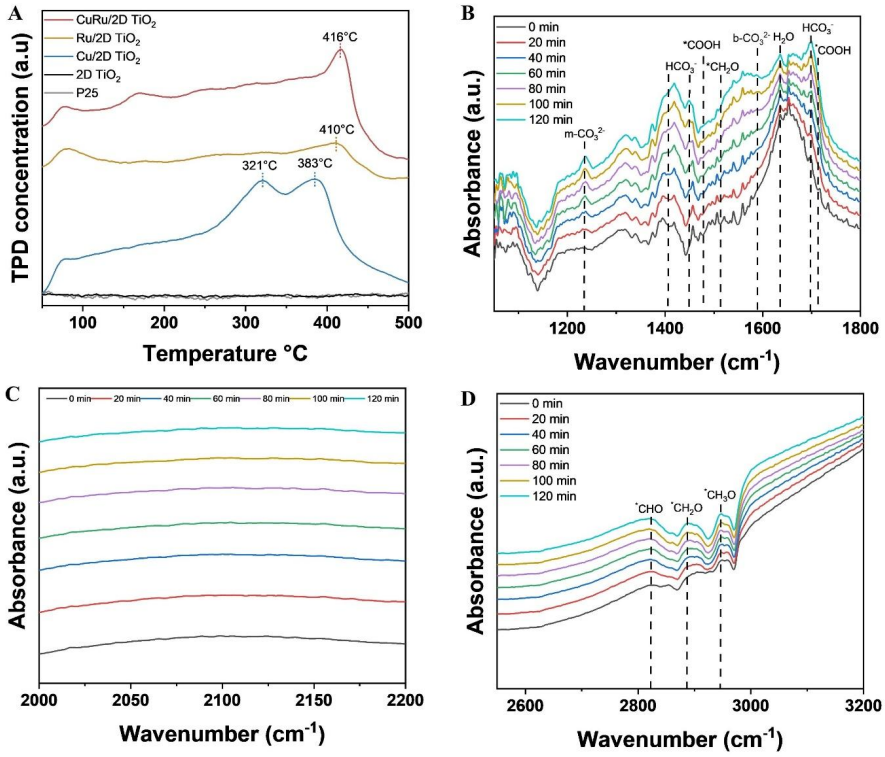


**Figure 6.** A, TPD analysis of P25, 2D $TiO_2$, Cu/2D $TiO_2$, Ru/2D $TiO_2$, and CuRu/2D $TiO_2$; B-D, *In situ* DRIFTS analysis of CuRu/2D $TiO_2$.

## CONCLUSIONS

This study demonstrates that Cu and Ru single atoms can be sequentially co-anchored on 2D $TiO_2$ nanosheets to form a photochemically active Cu/Ru dual single-atom catalyst for $CO_2$-to-$CH_4$ conversion. Structural characterization (XRD, XAFS, HAADF-STEM) confirms that both metals remain atomically dispersed in the fresh catalyst, with Cu present as $Cu^{2+}$ and Ru as $Ru^{4+}$ in oxygen-coordinated environments. Electronic and defect characterization (XPS, EPR, UV-Vis, PL) shows that co-loading Cu and Ru introduces an additional electronic interaction between the two metal sites together with more efficient suppression of radiative recombination.

The optimized Cu(0.8 wt.%)/Ru(0.6 wt.%) DSAC shows the highest $CH_4$ evolution rate among the catalysts examined, indicating both metals were predominantly stabilized as atomically dispersed species on $TiO_2$, thereby maximizing the number of accessible active sites. $^{13}CO_2$ labeling confirms that this $CH_4$ is derived from the gaseous $CO_2$ feed rather than adventitious surface carbon. *In situ* DRIFTS indicates that $CO_2$ reduction proceeds through carbonate/bicarbonate, *COOH, *CHO, *$CH_2O$, and *$CH_3O$

intermediates without observable *CO accumulation, consistent with a pathway toward deep hydrogenation to $CH_4$ rather than partial reduction to CO.

We demonstrate that the DSAC exhibits higher stability compared with the corresponding SAC by protecting against the loss of Cu active sites caused by excessive charge accumulation at Ru sites. However, partial reduction and aggregation of Ru into metallic species are still observed, indicating that further research is required to suppress Ru agglomeration in future studies. *Ex-situ* XAFS suggests a possible structural origin of this behavior: Cu remains atomically dispersed after reaction, whereas a fraction of Ru is reduced and aggregates into a metallic phase. This asymmetric degradation indicates that Ru stability, rather than Cu stability or overall $CO_2$ activation capacity, is a likely contributor limiting the long-term performance of this dual single-atom system.

These results show that pairing Cu and Ru single atoms on a 2D $TiO_2$ support is an effective strategy for enhancing $CO_2$ photoreduction activity relative to either single-atom catalyst alone. Cu/Ru DSACs supported on 2D $TiO_2$ nanosheets exhibited enhanced photocatalytic $CO_2$ reduction activity and stability through the synergistic interplay between atomically dispersed Cu and Ru sites. Cu-induced oxygen vacancies facilitated the stabilization of isolated Ru species while simultaneously promoting $CO_2$ adsorption, and the resulting dual-site structure further enhanced light harvesting and stabilized key reaction intermediates. At the same time, identifying Ru metallic bonding, which is a likely contributor to the observed deactivation pathway, defines a clear target for future catalyst design, such as protective coatings, alternative Ru coordination environments, or heterostructuring strategies previously shown to increase stability in related Cu-based $TiO_2$ photocatalysts. Addressing this stability limitation will be necessary before dual single-atom Cu/Ru-$TiO_2$ photocatalysts can be considered for practical solar $CO_2$ conversion.

## DECLARATIONS

### Acknowledgments

This research was supported by the National Research Foundation of Korea (NRF) funded by the Ministry of Science and ICT (RS-2026-25543401). The XAFS

experiments were conducted at the BL10C beamline in the Pohang Accelerator Laboratory.

## Authors' contributions

Conceptualization, Methodology, Visualization, Investigation, Formal analysis, Writing - review & editing, Writing - original draft: Lee J;

Conceptualization, Methodology, Visualization, Investigation, Formal analysis, Writing - review & editing: Kim DY;

Investigation, Formal analysis: Junho Lee, Investigation, Formal analysis: Chaitanya B. Hiragond, Investigation, Formal analysis: Eunhee Gong, Formal analysis: Zhu YF; Conceptualization, Writing - review & editing, Supervision, Resources, Project administration, Methodology, Investigation, Funding acquisition: In SI.

## Availability of data and materials

All relevant data are available in the main text and its supplemental information.

## Conflicts of interest

All authors declared that there are no conflicts of interest.

## Ethical approval and consent to participate

Not applicable.

## Consent for publication

Not applicable.

## Copyright



## REFERENCES

(1) Dong, C.; Lian, C.; Hu, S.; et al. Size-Dependent Activity and Selectivity of Carbon Dioxide Photocatalytic Reduction over Platinum Nanoparticles. *Nature Communications* **2018**, *9* (1).[DOI: 10.1038/s41467-018-03666-2]

(2) Wang, S.; Xu, M.; Peng, T.; et al. Porous Hypercrosslinked

Polymer-$TiO_2$-Graphene Composite Photocatalysts for Visible-Light-Driven $CO_2$ Conversion. *Nature Communications* **2019**, *10* (1).[DOI: 10.1038/s41467-019-08651-x]

(3) Chu, S.; Majumdar, A. Opportunities and Challenges for a Sustainable Energy Future. *Nature* **2012**, *488* (7411), 294-303.[DOI: 10.1038/nature11475]

(4) Armstrong, R. C.; Wolfram, C.; de Jong, K. P.; et al. The Frontiers of Energy. *Nature Energy* **2016**, *1* (1).[DOI: 10.1038/nenergy.2015.20]

(5) Fang, S.; Rahaman, M.; Bharti, J.; et al. Photocatalytic $CO_2$ Reduction. *Nature Reviews Methods Primers* **2023**, *3* (1).[DOI: 10.1038/s43586-023-00243-w]

(6) Ozin, G. Accelerated Optochemical Engineering Solutions to $CO_2$ Photocatalysis for a Sustainable Future. *Matter* **2022**, *5* (9), 2594-614.[DOI: 10.1016/j.matt.2022.07.033]

(7) Gong, E.; Ali, S.; Hiragond, C. B.; et al. Solar Fuels: Research and Development Strategies to Accelerate Photocatalytic $CO_2$ Conversion into Hydrocarbon Fuels. *Energy & Environmental Science* **2022**, *15* (3), 880-937.[DOI: 10.1039/D1EE02714J]

(8) Hiragond, C.; Powar, N.; In, S.-I. Recent Developments in Lead and Lead-Free Halide Perovskite Nanostructures towards Photocatalytic $CO_2$ Reduction. *Nanomaterials* **2020**, *10* (12), 2569.[DOI: 10.3390/nano10122569]

(9) Gong, E.; Kim, H.; Hiragond, C. B.; Lee, J.; Goddard III, W. A.; In, S.-I. Experimental and Machine Learning-Assisted Discovery of 2D Materials for Hydrogen Evolution: From Fundamentals to Industrial Applications. *EnergyChem* **2026**, *8* (5), 100206.[DOI: 10.1016/j.enchem.2026.100206]

(10) Scanlon, D. O.; Dunnill, C. W.; Buckeridge, J.; et al. Band Alignment of Rutile and Anatase $TiO_2$. *Nature Materials* **2013**, *12* (9), 798-801.[DOI: 10.1038/nmat3697]

(11) Collado, L.; Reynal, A.; Fresno, F.; et al. Unravelling the Effect of Charge Dynamics at the Plasmonic Metal/Semiconductor Interface for $CO_2$ Photoreduction. *Nature Communications* **2018**, *9* (1).[DOI: 10.1038/s41467-018-07397-2]

(12) Hou, W.; Cronin, S. B. A Review of Surface Plasmon Resonance-Enhanced Photocatalysis. *Advanced Functional Materials* **2012**, *23* (13), 1612-9.[DOI: 10.1002/adfm.201202148]

(13) Ji, Y.; Luo, Y. New Mechanism for Photocatalytic Reduction of $CO_2$ on the Anatase $TiO_2$ (101) Surface: The Essential Role of Oxygen Vacancy. *Journal of the American Chemical Society* **2016**, *138* (49), 15896-902.[DOI: 10.1021/jacs.6b05695]

(14) Wu, H.-Y.; Hon, M.-H.; Kuan, C.-Y.; Leu, I.-C. Preparation of TiO2(B) Nanosheets by a Hydrothermal Process and Their Application as an Anode for Lithium-Ion Batteries. *Journal of Electronic Materials* **2014**, *43* (4), 1048-54.[DOI: 10.1007/s11664-013-2951-y]

(15) Yang, J.; Wang, D.; Han, H.; Li, C. Roles of Cocatalysts in Photocatalysis and Photoelectrocatalysis. *Accounts of Chemical Research* **2013**, *46* (8), 1900-9.[DOI: 10.1021/ar300227e.

(16) Li, J.; Wang, S.; Li, R.; Zhang, B.; Xu, X.; Wang, Z.; Kang, L. Construction of Z-Scheme Photocatalyst with p-n Heterojunction of Molecular Semiconductors for Enhanced Photocatalytic Water Oxidation. *Applied Catalysis B: Environmental* **2024**, *342*, 123381.[DOI: 10.1016/j.apcatb.2023.123381]

(17) Hiragond, C.; Ali, S.; Sorcar, S.; In, S.-I. Hierarchical Nanostructured Photocatalysts for $CO_2$ Photoreduction. *Catalysts* **2019**, *9* (4), 370.[DOI: 10.3390/catal9040370]

(18) Ali, S.; Razzaq, A.; In, S.-I. Development of Graphene Based Photocatalysts for $CO_2$ Reduction to C1 Chemicals: A Brief Overview. *Catalysis Today* **2019**, *335*, 39-54.[DOI: 10.1016/j.cattod.2018.12.003]

(19) Razzaq, A.; Ali, S.; Asif, M.; In, S.-I. Layered Double Hydroxide (LDH) Based Photocatalysts: An Outstanding Strategy for Efficient Photocatalytic CO2 Conversion. *Catalysts* **2020**, *10* (10), 1185.[DOI: 10.3390/catal10101185]

(20) In, S.; Orlov, A.; García, F.; Tikhov, M.; Wright, D. S.; Lambert, R. M. Efficient Visible Light-Active N-Doped $TiO_2$ Photocatalysts by a Reproducible and Controllable Synthetic Route. *Chem. Commun.* **2006**, No. 40, 4236-8.[DOI: 10.1039/b610316b]

(21) In, S.; Orlov, A.; Berg, R.; García, F.; et al. Effective Visible Light-Activated B-Doped and B,N-Codoped $TiO_2$ Photocatalysts. *Journal of the American Chemical Society* **2007**, *129* (45), 13790-1.[DOI: 10.1021/ja0749237]

(22) Parayil, S. K.; Razzaq, A.; Park, S.-M.; Kim, H. R.; Grimes, C. A.; In, S.-I.

Photocatalytic Conversion of $CO_2$ to Hydrocarbon Fuel Using Carbon and Nitrogen Co-Doped Sodium Titanate Nanotubes. *Applied Catalysis A: General* **2015**, *498*, 205-213.[DOI: 10.1016/j.apcata.2015.03.044]

(23) Kim, K.; Razzaq, A.; Sorcar, S.; Park, Y.; Grimes, C. A.; In, S.-I. Hybrid Mesoporous $Cu_2ZnSnS_4$ (CZTS)-$TiO_2$ Photocatalyst for Efficient Photocatalytic Conversion of $CO_2$ into $CH_4$ under Solar Irradiation. *RSC Advances* **2016**, *6* (45), 38964-71.[DOI: 10.1039/c6ra02763f]

(24) Kim, H. R.; Razzaq, A.; Grimes, C. A.; In, S.-I. Heterojunction P-n-p $Cu_2O$/S-$TiO_2$ /CuO: Synthesis and Application to Photocatalytic Conversion of $CO_2$ to Methane. *Journal of $CO_2$ Utilization* **2017**, *20*, 91-6.[DOI: 10.1016/j.jcou.2017.05.008]

(25) Zubair, M.; Razzaq, A.; Grimes, C. A.; In, S.-I. $Cu_2ZnSnS_4$ (CZTS)-ZnO: A Noble Metal-Free Hybrid Z-Scheme Photocatalyst for Enhanced Solar-Spectrum Photocatalytic Conversion of $CO_2$ to $CH_4$. *Journal of $CO_2$ Utilization* **2017**, *20*, 301-311.[DOI: 10.1016/j.jcou.2017.05.021]

(26) Zubair, M.; Kim, H.; Razzaq, A.; Grimes, C. A.; In, S.-I. Solar Spectrum Photocatalytic Conversion of $CO_2$ to $CH_4$ Utilizing $TiO_2$ Nanotube Arrays Embedded with Graphene Quantum Dots. *Journal of $CO_2$ Utilization* **2018**, *26*, 70-9.[DOI: 10.1016/j.jcou.2018.04.004]

(27) Razzaq, A.; Grimes, C. A.; In, S.-I. Facile Fabrication of a Noble Metal-Free Photocatalyst: $TiO_2$ Nanotube Arrays Covered with Reduced Graphene Oxide. *Carbon* **2016**, *98*, 537-44.[DOI: 10.1016/j.carbon.2015.11.053]

(28) Kim, M.; Kim, Y. K.; Lim, S. K.; Kim, S.; In, S.-I. Efficient Visible Light-Induced $H_2$ Production by Au@CdS/$TiO_2$ Nanofibers: Synergistic Effect of Core-Shell Structured Au@CdS and Densely Packed $TiO_2$ Nanoparticles. *Applied Catalysis B: Environmental* **2015**, *166-167*, 423-31.[DOI: 10.1016/j.apcatb.2014.11.036]

(29) Razzaq, A.; Sinhamahapatra, A.; Kang, T.-H.; Grimes, C. A.; Yu, J.-S.; In, S.-I. Efficient Solar Light Photoreduction of $CO_2$ to Hydrocarbon Fuels via Magnesiothermally Reduced $TiO_2$ Photocatalyst. *Applied Catalysis B: Environmental* **2017**, *215*, 28-35.[DOI: 10.1016/j.apcatb.2017.05.028]

(30) Hiragond, C. B.; Lee, J.; Kim, H.; et al. A Novel N-Doped Graphene Oxide

Enfolded Reduced Titania for Highly Stable and Selective Gas-Phase Photocatalytic $CO_2$ Reduction into $CH_4$: An in-Depth Study on the Interfacial Charge Transfer Mechanism. *Chemical Engineering Journal* **2021**, *416*, 127978.[DOI: 10.1016/j.cej.2020.127978]

(31) Yang, W.; Kim, D.; Lee, G.; et al. Selective Conversion of $CO_2$ to CO Using Blue $TiO_2$ with an R-GO Shell and Quantitative Measurement of Excited Electrons with Four-Wave Mixing Microspectroscopy. *Carbon* **2025**, *232*, 119819.[DOI: 10.1016/j.carbon.2024.119819]

(32) Hwang, Y.; Sorcar, S.; Lee, J.; Jung, J.; Cho, C.; In, S. Reduced $TiO_2$ Quantum Dots/Graphene for Solar Light Driven $CO_2$ Reduction into Precisely Controlled C1 vs C2 Hydrocarbon Products without Noble Co-Catalyst. *Journal of Power Sources* **2023**, *556*, 232430.[DOI: 10.1016/j.jpowsour.2022.232430]

(33) Xue, Z.-H.; Luan, D.; Zhang, H.; (David) Lou, X. W. Single-Atom Catalysts for Photocatalytic Energy Conversion. *Joule* **2022**, *6* (1), 92-133. https://doi.org/10.1016/j.joule.2021.12.011]

(34) Liu, L.; Corma, A. Metal Catalysts for Heterogeneous Catalysis: From Single Atoms to Nanoclusters and Nanoparticles. *Chemical Reviews* **2018**, *118* (10), 4981-5079. https://doi.org/10.1021/acs.chemrev.7b00776]

(35) Hiragond, C. B.; Powar, N. S.; Lee, J.; In, S. Single-Atom Catalysts (SACs) for Photocatalytic $CO_2$ Reduction with $H_2O$: Activity, Product Selectivity, Stability, and Surface Chemistry. *Small* **2022**, *18* (29).[DOI: 10.1002/smll.202201428]

(36) Ross, M. B.; De Luna, P.; et al. Designing Materials for Electrochemical Carbon Dioxide Recycling. *Nature Catalysis* **2019**, *2* (8), 648-58.[DOI: 10.1038/s41929-019-0306-7]

(37) Lee, B.-H.; Gong, E.; Kim, M.; et al. Electronic Interaction between Transition Metal Single-Atoms and Anatase $TiO_2$ Boosts $CO_2$ Photoreduction with $H_2O$. *Energy Environ. Sci.* **2022**, *15* (2), 601-9.[DOI: 10.1039/d1ee01574e]

(38) Wang, T.; Sun, F.; Liu, S.; Zhuang, G.; Li, B. Dioxygen-Enhanced $CO_2$ Photoreduction on $TiO_2$ Supported Cu Single-Atom Sites. *Applied Catalysis B: Environmental* **2023**, *325*, 122339.[DOI: 10.1016/j.apcatb.2022.122339]

(39) Hiragond, C. B.; Biswas, S.; Powar, N. S.; et al. Surface-modified Ag@Ru-P25 for Photocatalytic $CO_2$ Conversion with High Selectivity over $CH_4$ Formation at the Solid-Gas Interface. *Carbon Energy* **2023**, *6* (1).[DOI: 10.1002/cey2.386]

(40) Cánovas, M. A.; Gracia, A.; Sayós, R.; Gamallo, P. $CO_2$ Hydrogenation on Ru Single-Atom Catalyst Encapsulated in Silicalite: A DFT and Microkinetic Modeling Study. *The Journal of Physical Chemistry C* **2024**, *128* (39), 16551-62.[DOI: 10.1021/acs.jpcc.4c05941]

(41) Hung, S.-F.; Xu, A.; Wang, X.; et al. A Metal-Supported Single-Atom Catalytic Site Enables Carbon Dioxide Hydrogenation. *Nature Communications* **2022**, *13* (1).[DOI: 10.1038/s41467-022-28456-9]

(42) Wu, Q.; Shen, C.; Rui, N.; Sun, K.; Liu, C. Experimental and Theoretical Studies of $CO_2$ Hydrogenation to Methanol on $Ru/In_2O_3$. *Journal of CO2 Utilization* **2021**, *53*, 101720.[DOI: 10.1016/j.jcou.2021.101720]

(43) Wang, C.; Lu, Y.; Zhang, Y.; et al. Ru-Based Catalysts for Efficient $CO_2$ Methanation: Synergistic Catalysis between Oxygen Vacancies and Basic Sites. *Nano Research* **2023**, *16* (10), 12153-64.[DOI: 10.1007/s12274-023-5592-3]

(44) Lee, C. W.; Lee, B.-H.; Park, S.; et al. hotochemical Tuning of Dynamic Defects for High-Performance Atomically Dispersed Catalysts. *Nature Materials* **2024**, *23* (4), 552-9.[DOI: 10.1038/s41563-024-01799-y]

(45) Kim, D.; Lee, K.; Park, Y. H.; et al. Enhancing $CO_2$-to-$CH_4$ Conversion Efficiency of $TiO_2$ through Synergistic Morphology Tuning, Defect Engineering, and Heterojunction Formation. *Chemical Engineering Journal* **2026**, *527*, 171564.[DOI: 10.1016/j.cej.2025.171564]

(46) Kim, D.; Ko, W.; Lee, B.; et al. Atomic Tuning of Metal-Support Interactions for Pathway-Selective $CO_2$ Photoreduction on $TiO_2$. *Advanced Science* **2026**.[DOI: 10.1002/advs.202521625]

(47) Lee, B.-H.; Park, S.; Kim, M.; et al. Reversible and Cooperative Photoactivation of Single-Atom $Cu/TiO_2$ Photocatalysts. *Nature Materials* **2019**, *18* (6), 620-6.[DOI: 10.1038/s41563-019-0344-1]

(48) In, S.; Vaughn, D. D.; Schaak, R. E. Hybrid CuO-$TiO_{2-x}N_x$ Hollow Nanocubes for

Photocatalytic Conversion of $CO_2$ into Methane under Solar Irradiation. *Angewandte Chemie International Edition* **2012**, *51* (16), 3915-8.[DOI: 10.1002/anie.201108936]

(49) Zhang, H.; Zuo, S.; Qiu, M.; et al. Direct Probing of Atomically Dispersed Ru Species over Multi-Edged $TiO_2$ for Highly Efficient Photocatalytic Hydrogen Evolution. *Science Advances* **2020**, *6* (39).[DOI: 10.1126/sciadv.abb9823]

(50) Zhang, Y.; Zhao, J.; Wang, H.; et al. Single-Atom Cu Anchored Catalysts for Photocatalytic Renewable $H_2$ Production with a Quantum Efficiency of 56%. *Nature Communications* **2022**, *13* (1).[DOI: 10.1038/s41467-021-27698-3]

(51) Xiao, B.; Shen, C.; Luo, Z.; et al. Cu Surface Doped $TiO_2$: Constructing Cu Single-Atoms Active Sites and Broadening the Photo-Response Range for Efficient Photocatalytic Hydrogen Production. *Chemical Engineering Journal* **2023**, *468*, 143650.[DOI: 10.1016/j.cej.2023.143650]

(52) Cheng, C.; Fang, W.-H.; Long, R.; Prezhdo, O. V. Water Splitting with a Single-Atom Cu/$TiO_2$ Photocatalyst: Atomistic Origin of High Efficiency and Proposed Enhancement by Spin Selection. *JACS Au* **2021**, *1* (5), 550-9.[DOI: 10.1021/jacsau.1c00004]

(53) Xin, X.; Xu, T.; Yin, J.; Wang, L.; Wang, C. Management on the Location and Concentration of $Ti^{3+}$ in Anatase $TiO_2$ for Defects-Induced Visible-Light Photocatalysis. *Applied Catalysis B: Environmental* **2015**, *176-177*, 354-62.[DOI: 10.1016/j.apcatb.2015.04.016]

(54) Kim, H.-J.; Mori, K.; Ichikawa, S.; Nakano, T.; Yamashita, H. Layered $Na_2Ti_3O_7$-Supported Ru Catalyst for Ambient $CO_2$ Methanation. *Nature Communications* **2025**, *16* (1).[DOI: 10.1038/s41467-025-57954-9]

(55) Kibria, M. G.; Chowdhury, F. A.; Zhao, S.; et al. Visible Light-Driven Efficient Overall Water Splitting Using p-Type Metal-Nitride Nanowire Arrays. *Nat Commun* **2015**, *6* (1), 6797.[DOI: 10.1038/ncomms7797]

(56) Liu, K.; Sun, Z.; Peng, X.; et al. Tailoring Asymmetric RuCu Dual-Atom Electrocatalyst toward Ammonia Synthesis from Nitrate. *Nature Communications* **2025**, *16* (1).[DOI: 10.1038/s41467-025-57463-9]

(57) Ali, S.; Kim, D.; Gong, E.; et al. Copper Deposited on Reduced Titania as Catalyst

for the Production of $CH_4$ from Sunlight and Air. *ChemCatChem* **2024**, *16* (18).[DOI: 10.1002/cctc.202301485]

(58) Feng, C.; Hu, M.; Zuo, S.; et al. Ru-$O_V$ Site-Mediated Product Selectivity Switch for Overall Photocatalytic $CO_2$ Reduction. *Advanced Materials* **2024**, *37* (5).[DOI: 10.1002/adma.202411813]

(59) Gong, E.; Kim, H. R.; Hwang, Y.; et al. Revealing the Structure-Activity Relationship of $Mn_3O_4/TiO_2$ via Phase Engineering for Enhanced Photocatalytic $CO_2$ Reduction. *Journal of CO2 Utilization* **2026**, *105*, 103357.[DOI: 10.1016/j.jcou.2026.103357]

(60) Powar, N. S.; Kim, S.; Lee, J.; et al. Unravelling the Effect of $Ti^{3+}/Ti^{4+}$ Active Sites Dynamic on Reaction Pathways in Direct Gas-Solid-Phase $CO_2$ Photoreduction. *Applied Catalysis B: Environment and Energy* **2024**, *352*, 124006.[DOI: 10.1016/j.apcatb.2024.124006]

(61) Hiragond, C. B.; Prakash, P.; Das, T.; et al. Highly Selective $CO_2$-to-$CH_4$ Conversion via Multisun-Assisted Photocatalysis Enabled by Dual Cocatalyst Interfaces. *Applied Catalysis B: Environment and Energy* **2026**, *399*, 127142.[DOI: 10.1016/j.apcatb.2026.127142]

(62) Powar, N. S.; Jang, M.; Gyu Kim, M.; et al. Dynamic $Ti^{3+}$ and $In^{3+}$ Dual Active Sites on $In_2TiO_5$ to Enhance Visible-Light-Driven Gas-Phase Photocatalytic $CO_2$ Reduction. *Chemical Engineering Journal* **2024**, *480*, 147966.[DOI: 10.1016/j.cej.2023.147966]

(63) Powar, N. S.; Kwon, S.; Hiragond, C. B.; et al. Defect-Driven Dynamics in Gas-Phase Photocatalytic $CO_2$ Conversion to Solar Fuels Using $Ti^{3+}/Ti^{4+}$ Containing $TiO_2$ and Nonstoichiometric $Ag_2S$ Nanowires. *ACS Catal.* **2025**, *15* (21), 18474-83.[DOI: 10.1021/acscatal.5c05258]